

An experimental study on the deformation and fracture modes of steel projectiles during impact

K.G. Rakvåg^{a,*}, T. Børvik^{a,b}, I. Westermann^{a,c} and O.S. Hopperstad^a

^a *Structural Impact Laboratory (SIMLab), Centre for Research-based Innovation (CRI) and Department of Structural Engineering, Norwegian University of Science and Technology, NO-7491 Trondheim, Norway*

^b *Norwegian Defence Estates Agency, Research & Development Department, NO-0103 Oslo, Norway*

^c *SINTEF Materials & Chemistry, NO-7465 Trondheim, Norway*

Abstract

Previous investigations of the penetration and perforation of high-strength steel plates struck by hardened steel projectiles have shown that under certain test conditions the projectile may fracture or even fragment upon impact. Simulations without an accurate failure description for the projectile material will then predict perforation of the target instead of fragmentation of the projectile, and thus underestimate the ballistic limit velocity of the target plate. This paper presents an experimental investigation of the various deformation and fracture modes that may occur in steel projectiles during impact. This is studied by conducting Taylor bar impact tests using 20 mm diameter, 80 mm long, tool steel projectiles with three different hardness values (HRC 19, 40 and 52). A gas gun was used to fire the projectiles into a rigid wall at impact velocities ranging from 100 – 350 m/s, and the deformation and fracture processes were captured by a high-speed video camera. From the tests, several different deformation and fracture modes were registered for each hardness value. To investigate the influence of material on the deformation and fracture modes, several series of tensile tests on smooth axisymmetric specimens were carried out to characterise the mechanical properties of the three materials. To gain a deeper understanding of the various processes causing fracture and fragmentation during impact, a metallurgical investigation was conducted. The fracture surfaces of the failed projectiles of different hardness were investigated, and the microstructure was studied for each hardness value.

Keywords: Taylor bar impact tests; fracture; fragmentation; material tests; metallurgical study

* Corresponding author: Tel.: +47 73 59 52 02; fax: +47 73 59 47 01.
E-mail address: knut.gaarder.rakvag@ntnu.no (K.G. Rakvåg)

1 Introduction

Previous investigations [1][2][3] on the penetration and perforation of high-strength steel plates with different thicknesses struck by hardened steel projectiles at various impact velocities have shown that under certain test conditions the projectile may fracture or even fragment upon impact. Numerical simulations without a proper failure description for the projectile material will then predict perforation of the target instead of fragmentation of the projectile, and thus underestimate the ballistic limit velocity of the target plate. This may cause very misleading results in computer-aided design of protective structures [4].

In this study, the classical Taylor bar impact test will be used to provoke fracture and fragmentation in the projectile. The test was originally conceived in 1948 by Taylor [5], Whiffin [6] and Carrington and Gayler [7] as a material test to determine the dynamic compressive yield stress of metallic materials. The test procedure is to impact a blunt-nose projectile into a rigid wall, and based on post-impact measurements of the deformed cylinder, material properties are extracted based on Taylor's analysis [5]. It has later been shown that the Taylor bar impact test is not suitable as a material characterization test. The results from the Taylor analysis are at best approximations, and it has been shown through experiments and numerical simulations that the analysis neither predicts the deformation nor the dynamic yield strength accurately (see e.g. [8]). Hence, the Taylor bar impact test is used herein as a component test, while tension tests are used to characterise the material properties.

Well over 400 scientific articles have been published with relation to the Taylor test [9], but only a few have investigated fracture or fragmentation of the projectile in any detail. Still, studies like Backman and Goldsmith [10], Woodward et al. [11] and Chen et al. [12] have revealed five distinct deformation and fracture modes in the projectile during Taylor bar impact tests for steels, as illustrated in Figure 1. These are a) Mushrooming without any visible cracking, b) Tensile splitting on the edge of the mushroomed end due to tensile hoop strains exceeding the material ductility, c) Adiabatic shear cracking either by 1) principal shear fracture where a circular wedge separates (denoted as a cone in [11]) or 2) combined spiral shear fracture and tensile splitting where the mushroomed material separates from the impact end of the projectile, d) Full fragmentation initiated by crack growth from one or several shear cracks and e) Extensive petalling initiated by tensile splitting (denoted sunflower-like petalling in [12]) that may cause fragmentation of the petals at the highest impact velocities. A further failure mode mentioned in the literature during Taylor bar impact tests is extensive void growth and severe damage, just behind the centre of impact due to hydrostatic tension in the centre of the

projectile [11]. Combinations of two or several of the mentioned distinct modes are possible in real situations.

Chen et al. [12] performed a study on soft steel projectiles impacting a harder, but not rigid, target plate with velocities ranging from 200 – 800 m/s. They observed extensive petalling in the projectile, but also another important difference between the standard Taylor test and their own non-penetrating experiments. With a deformable target plate the mushroomed part of the impact end of the projectile consisted of two parts: An inner circle with diameter approximately equal to the un-deformed projectile diameter and an outer loop of material. The tensile splitting in the outer loop never crossed the interface between the parts and based on this observation they concluded that the reason for the petalling is the separation of the outer loop from the inner circle.

Xiao et al. [14] performed experiments on projectiles of two different hardness values (HRC 20 and 52). They observed mushrooming and shear cracking in both projectiles. Petalling was also identified for the soft projectiles, while fragmentation occurred for the hard projectiles. For the mushrooming they experienced the same inner and outer loop pattern as Chen et al. [12] due to a small indentation in the target plate, even though the target plate was harder than the projectile. These results highlighted another issue of the Taylor test, namely that the analysis requires the target plate to remain fully rigid and a flat plane during impact. Furthermore, the shear fracture modes were different for the two projectile types. For the soft projectiles the mode was equal to spiral shear, while for the hard projectiles it was equal to principal shear. In a subsequent paper, Xiao et al. [15] speculated that the fracture mechanism for shear cracking and fragmentation is the same based on numerical simulations of a high-strength aluminium alloy. Ren et al. [16] observed in experiments on aluminium projectiles that the spiral shear cracks self-organize in a symmetrical pattern. Using SEM fractography they observed three distinct fracture surfaces. Both ductile dimples and a more smeared surface were seen for the lower impact velocities causing fracture, but when the velocity was increased they also observed melted and solidified material which they attributed to adiabatic shear bands.

In design of protective structures the critical impact velocity for fracture or fragmentation of the projectile is of special interest. When the projectile fragments it loses most of its penetrating capacity. Thus, incorporating the deformation and fracture behaviour of impacting projectiles is crucial in design [4]. The aim of this work is to investigate experimentally the deformation and fracture modes occurring in steel projectiles during impact. This is studied by conducting Taylor bar impact tests using 20 mm diameter, 80 mm long, Arne tool steel projectiles with three different hardness values (HRC 19, 40 and 52). A compressed gas gun

was used to fire the projectiles into a rigid wall at impact velocities ranging from 100 – 350 m/s, and the deformation and fracture processes were captured by a high-speed video camera. From each test, the different fracture and fragmentation modes were registered. Several series of tensile tests on smooth axisymmetric specimens taken from the projectiles both before and after hardening were carried out to characterise the material properties. To gain a deeper understanding of the various processes causing fracture and fragmentation in the projectiles during impact, some of the projectiles were subjected to a metallurgical investigation.

2 Experimental procedure

2.1 Compressed gas-gun facility

A compressed gas-gun facility was used to accelerate the projectiles. The test rig is a slightly modified version of the one described in [1] and is sketched in Figure 2. In these tests air was used as propellant, limiting the impact velocity to the speed of sound in air at room temperature (i.e. $v_i \approx 350$ m/s). Before testing, the projectile was mounted in a sabot and inserted into the barrel. Membranes of varying thickness according to the applied air pressure were used to separate the firing section from the pressure tank and the barrel. Compressed air of pressures up to 50 bars was pumped into the pressure tank and firing section, with half the pressure in the latter. The gun was fired with a rapid evacuation of the firing section, which led to a doubling of the pressure gradient over the membranes. Thus, the membranes failed successively and the sabot package with the projectile was accelerated throughout the barrel. Upon entering the impact chamber the sabot was removed from the projectile due to the aerodynamic forces and stopped by a sabot trap. The projectile moved unaffected through the sabot trap and a velocity measurement station, which also triggered some flash lamps and a Photron FASTCAM SA1.1 high-speed video camera mounted outside the impact chamber. In these tests, the high-speed video system was operating at a framing rate of approximately 100.000 fps.

2.2 Projectiles

The projectiles used in this study are all made of Arne tool steel manufactured by Uddeholms AB in Sweden. The nominal chemical composition of the material is given in Table 1. After careful machining to cylinders with nominal diameter 20 mm, length 80 mm and mass 197 grams, series of projectiles were heat-treated to acquire three different hardness values. The

first series of projectiles was unhardened (UH), i.e. they were used in the soft annealed condition. The hardness in this condition corresponds to HRC 19. The second series of projectiles was hardened to HRC 40, while the third series of projectiles was hardened to HRC 52. The heat-treatment processes are described in Table 2. The obtained hardness was then controlled in a Rockwell C hardness testing device. Based on 6 indentations on the surface of each projectile the average hardness was found to HRC 37.8 (with a standard deviation of 1.2) and HRC 52.4 (with a standard deviation of 1.5) for series 2 and 3, respectively. Test data from tensile tests on specimens taken both before and after hardening will be presented in Section 4.

2.3 Target plate

The target plates were manufactured to be as rigid as possible, i.e. bulky and elastic, but not so hard and brittle that they would fracture upon impact. After some trial tests, they were chosen to have a diameter of 100 mm and a thickness of 50 mm, and were made of tool steel hardened to HRC 60. The target plates were supported by thick high-strength steel plates (see Figure 2), and no visual deflection of the fixture was detected in any of the high-speed video recordings. The tests with the highest impact velocities and the hardest projectiles left a small indentation in the target plates, so they were turned and/or rotated after each experiment so that the projectile always hit a virgin surface. The target plates were replaced when cracks were observed, typically after 4-5 impacts.

2.4 Experimental programme

The experimental programme consisted of Taylor bar impact tests with striking velocities ranging from about 100 to 350 m/s for each material. The variation in velocity and material properties allowed for a range of failure modes. All materials were impacted at velocities from 150 m/s to 300 m/s in 50 m/s intervals. The remaining projectiles were then impacted at velocities that were deemed interesting for each material based on the fixed interval tests. In total 22 tests were carried out (6 tests with unhardened projectiles, 8 tests with projectiles hardened to HRC 40 and 8 tests with projectiles hardened to HRC 52).

3 Experimental results

Typical high-speed video images from Taylor bar impact tests with projectiles having different hardness are shown in Figure 3. Since the impact velocity is about the same in all these

tests ($v_i \approx 300$ m/s), the difference in deformation and fracture modes with projectile hardness is clearly illustrated. For the unhardened projectile, considerable mushrooming and shortening without fracture are seen. For the projectile hardened to HRC 40, both spiral shear cracking and tensile splitting are observed, in addition to mushrooming. For the HRC 52 projectile, initial mushrooming is soon overtaken by fragmentation and the projectile is completely shattered into a large number of fragments.

Some of the main experimental results are summarized in Table 3. For the projectiles that did not fracture, the deformed length and mushroom diameter are listed, while for the projectiles that fractured only the dominating fracture mode is given. The fragment-size distribution in weight % of the total mass for the projectiles that fractured during impact is listed in Table 4. From these tables the change in deformation mode from mushrooming to fracture with projectile hardness and impact velocity is easily recognised. Note also that minor pitch and yaw angles (less than $1-2^\circ$) were observed in some of the tests, i.e. the impact was not completely head-on. Such small angles are almost impossible to avoid using free-flying projectiles. However, they are not considered of major importance in this study where fracture and fragmentation in the projectile is the main topic. Characteristics and observations for each deformation and fracture mode are discussed below.

3.1 Mushrooming

Mushrooming is characterized by plastic deformation without any visible cracks. The highest impact velocity obtained in this experimental programme without any visible exterior cracks was 297.2 m/s for the unhardened projectiles, 246.5 m/s for the HRC 40 projectiles and 124.4 m/s for the HRC 52 projectiles. Needless to say the plastic deformation varied considerably in this range of impact velocities and material properties. A summary of the post-impact length and mushroom diameter for the mushroomed projectiles is presented in Table 3, while Figure 4 shows a picture of a typical mushroomed projectile after impact.

3.2 Void nucleation

The unhardened projectile that impacted at a velocity of 297.2 m/s, i.e. the highest impact velocity without any visible exterior cracks, was split in the longitudinal direction to check for voids. As shown in Figure 5a) there is no evidence of voids that have nucleated and grown to detectable sizes. There are some spots that could be interpreted as voids, but it is difficult to

distinguish them from sulphides that may have disappeared due to the etching during preparation of the specimen. Evidence of a deformed sulphide that has partly dissolved from the etching process during preparation is shown in Figure 5b).

3.3 *Tensile splitting*

There was only one instance of tensile splitting as the exclusive fracture mode observed in this experimental programme. That happened for a HRC 40 projectile impacting the rigid plate at a velocity of 269.6 m/s. At this velocity only one single crack appeared at the rim of the projectile. Other deformation and fracture modes were seen at lower ($v_i = 246.5$ m/s) or higher ($v_i = 297.7$ m/s) impact velocities.

3.4 *Principal shear crack*

A fracture dominated by a principal shear crack was obtained in the HRC 52 projectiles at low impact velocities. An image just after impact from the high-speed video of the HRC 52 projectile that struck at 132.9 m/s is shown in Figure 6. It is evident that the fracture mode is principal shear as also identified by Woodward et al. [11]. Here, the cylindrical projectile is cut by a shear plane intersecting with the flat end of the projectile. Thus, a cylindrical wedge-shaped fragment is created. The same type of fracture mechanism is also present in the HRC 52 projectile that impacted at 134.7 m/s (see Figure 7). Here, also a secondary shear crack occurred approximately 90 degrees to the primary shear crack. The result is a projectile with a wedge-shaped tip after impact.

3.5 *Spiral shear and tensile splitting*

A combination of spiral shear and tensile splitting due to hoop tension was obtained in both unhardened and HRC 40 projectiles when the impact velocity was increased. For the unhardened projectiles, only the projectile with the highest impact velocity fractured in this mode, while this happened in the velocity range $297.7 \leq v_i \leq 356.5$ m/s for the HRC 40 projectiles.

The unhardened projectile at $v_i = 341.4$ m/s is shown in Figure 8. When looking at the projectile from the impacted end the cracks seem to initiate at the rim of the projectile and propagate radially towards the centre of the circular cross-section. However, when viewed from

the opposite direction it is clear that the cracks expand like a helicoid in the longitudinal direction. A HRC 40 projectile at $v_i = 297.7$ m/s with the same fracture mode is shown in Figure 9. The amount of damage in the projectile is very similar to the unhardened projectile that impacted the target at approximately 50 m/s higher velocity.

3.6 *Fragmentation*

All HRC 52 projectiles that impacted the target at impact velocities equal to or higher than 153.7 m/s fragmented in such a way that the entire front of the projectile was totally disintegrated. With increased impact velocity the number of fragments increased, while the size of the fragments and the remaining longitudinal section of the projectile that did not shatter decreased (see also Table 4). The fragments from a HRC 52 projectile after impact at a velocity of 250.5 m/s are shown in Figure 10. A typical fragmentation process during impact is shown in Figure 3c).

3.7 *Other observations*

An interesting observation is the evidence of blue brittleness in some of the projectiles. Blue brittleness is caused by a release of second-order particles in the material at temperatures of about 300°C [17][18]. This results in decreased ductility and increased strength (causing a decrease in impact resistance) in this temperature region, and the phenomenon is identified by a blue colour shade in the metal, as shown in Figure 8 and Figure 9. Another interesting observation in this context is that this seems to coincide with the appearance of cracks. Figure 4 shows pictures of the unhardened projectile at the highest impact velocity without any visible cracks or blue brittleness, in contrast to Figure 8 where both cracks and blue brittleness are observed. As thermal recordings are difficult in high-velocity impact events, the evidence of blue brittleness can be used to say something about the temperature in the projectiles at the highest velocities, and also about the spatial variation of the temperature, owing to the fact that only the centre of the projectile is shaded blue (indicating blue brittleness).

4 Material tests

4.1 Quasi-static tensile tests

Several series of tension tests were performed with smooth axisymmetric specimens to characterize the flow and failure properties of the materials. The geometry of the samples is given in Figure 11a) and conforms to ISO 6892-1:2009 [19]. Firstly, three parallel tests were carried out at quasi-static strain rate and room temperature on specimens cut directly from projectiles with different hardness values (i.e. UH, HRC 40 and HRC 52). The cross-head velocity of the tension machine was 1.2 mm/min in all tests, corresponding to an average strain rate of $5 \times 10^{-4} \text{ s}^{-1}$ in the gauge area before necking. During testing, the force and the diameter at minimum cross-section of the specimen were measured continuously until fracture. The latter was made possible using an in-house measuring rig with two perpendicular lasers that accurately measured the specimen diameter. Each laser projected a beam with dimension $13 \times 0.1 \text{ mm}^2$ towards the detector on the opposite side of the specimen. Thus, the two orthogonal lasers created a box of laser light of $13 \times 13 \times 0.1 \text{ mm}^3$ around the minimum cross-section of the sample. As the specimen was deformed, the continuous change in diameters was observed by the detectors. This dual-axis micrometer was made up of a high-speed, contactless AEROEL XLS13XY laser gauge with $1 \text{ }\mu\text{m}$ resolution, which was installed on a mobile frame to ensure that the diameters always were measured at minimum cross-section. During elongation, the sample was scanned at a frequency of 1200 Hz and the measured data were transferred by the built-in electronics to the remote computer via fast Ethernet.

From the two perpendicular diameter measurements, denoted D_1 and D_2 in this study, the effective area is approximated as

$$A = \frac{\pi}{4} D_1 D_2 \quad (1)$$

The Cauchy (true) stress is then given as

$$\sigma = \frac{F}{A} \quad (2)$$

Since some of these materials exhibit rather brittle behaviour, the elastic strain cannot be neglected in the calculation of the logarithmic (true) strain. The true radial (transverse) strain which in general consists of an elastic and plastic part may be calculated as

$$\varepsilon_r = \varepsilon_r^e + \varepsilon_r^p = \ln \frac{D}{D_0} \quad (3)$$

where D_0 is the initial diameter of the specimen and $D = \sqrt{D_1 D_2}$. The elastic and plastic parts of the radial strain are related to the longitudinal strain ε_l through Poisson's ratio ν and plastic incompressibility, i.e.

$$\ln \frac{D}{D_0} = -\nu \varepsilon_l^e - \frac{1}{2} \varepsilon_l^p = -\nu \varepsilon_l^e - \frac{1}{2} (\varepsilon_l - \varepsilon_l^e) \quad (4)$$

Solving this equation for the longitudinal strain yields

$$\varepsilon_l = 2 \ln \frac{D_0}{D} + (1 - 2\nu) \varepsilon_l^e \quad (5)$$

The elastic longitudinal strain is given from the stress by Hooke's law and the longitudinal strain becomes

$$\varepsilon_l = \ln \frac{A_0}{A} + (1 - 2\nu) \frac{\sigma}{E} \quad (6)$$

where $A_0 = \frac{\pi}{4} D_0^2$ is the initial area of the specimen.

Measured true stress-strain curves from the tensile tests on specimens cut from unhardened projectiles are shown in Figure 12, while similar curves are shown with blue dashed lines in Figure 13 for specimens cut from projectiles hardened to HRC 40 and in Figure 14 for specimens cut from projectiles hardened to HRC 52. The unhardened projectiles show no variation in yield stress or strain hardening, but some variation in strain to failure. This variation is however low compared to the variation in failure strain observed for the specimens cut from projectiles hardened to HRC 40. Further, the specimens cut from projectiles hardened to HRC

52 have a variation in strain to failure of the same order as the failure strain itself, in addition to a considerable variation in the yield stress. From these figures it is seen that the yield stress and the variation in material properties increase with increasing material hardness, whereas the strain hardening and strain to failure decrease.

Secondly, based on these observations it was decided to conduct a larger investigation of the hardened materials. In an attempt to sample the properties of the hardened materials, opposed to the bulk properties of the projectiles, the test specimens for this second study were first cut from unhardened projectiles and then hardened to the desired hardness values. The heat-treatment processes applied to the tensile test specimens are given in Table 5, and some differences compared to those for the projectiles (Table 2) are seen. As the tensile test specimens are considerably more slender (6 mm) than the projectiles (20 mm), the cooling of the test specimens will be faster and more uniform, thus assumed to give a more ideal representation of the nominal mechanical behaviour. To get an idea of the statistical distribution of the material properties, 20 tests from each material were carried out. The true stress-strain curves from these tests are shown with red solid lines in Figure 13 (HRC 40) and Figure 14 (HRC 52), where they are compared to the test results from the first series of tensile tests. It is seen that the test specimens first cut and then hardened have a substantially different behaviour than those cut directly from hardened projectiles. The assumed more ideal representation of the HRC 40 material is more ductile than the bulk-hardened material, with both a lower yield stress and a higher fracture strain. The HRC 52 material exhibits significantly higher fracture strains than the bulk-hardened material, and almost no variation in the yield stress or strain hardening. However, the variation in strain to failure for this material is considerable. This illustrates the stochastic nature of the problem.

It was speculated that the variation of the yield stress and strain to failure in the bulk-hardened HRC 52 test specimens could be due to micro-cracks in the surface originating from the manufacturing process. To investigate this, five more specimens were tested. These were manufactured in the same way as the initial test specimens, i.e. cut from an already hardened projectile. To limit possible micro-cracks the test specimens were carefully polished with 4000 sandpaper in the gauge area prior to testing. However, as shown in Figure 14 where the stress-strain curves from these tensile tests are shown with black dash-dotted lines, the material behaviour of polished specimens is comparable to the data from the first test series. As a matter of fact, the strain to failure seems to decrease somewhat, but owing to the low number of test specimens this trend may not be statistically significant. The three initial test specimens and the five polished specimens could thus be assumed as representative of the same material

behaviour. As will be shown in the next section, carbides and intermetallic inclusions are randomly distributed in the hardened material. This may explain the large scatter in the fracture stress seen in Figure 14.

Based on the marked difference in material behaviour between the test specimens first hardened then cut and the test specimens first cut then hardened it seems possible that the material properties are distributed spatially as a function of the distance to the surface due to the uneven cooling during production. This conjecture will be investigated in the next section through hardness testing. In addition, due to the variation of the material properties not only between the test series, but between parallel tests as well, one should also consider the properties of the hardened material as random variables with a probability distribution given by the material tests.

4.2 *Dynamic tensile tests*

Due to the extreme strain rates involved in Taylor bar impact tests, the quasi-static test programme was expanded with tension tests at high strain rates in a Split-Hopkinson tension bar (SHTB) system (see e.g. [20]). This setup was used for 6 tests of the unhardened material with strain rates ranging from 53 to 861 s⁻¹. The axisymmetric specimen geometry is shown in Figure 11b). The relevant standard, ISO 26203-1:2010 [21], covers only sheet materials in detail but allows for other geometries than the flat test samples considered therein. The axisymmetric specimen geometry used here has been successfully used in previous studies, see e.g. [17] and [20]. Tests at elevated strain rates were only done for the unhardened material since the strain-rate sensitivity is believed to decrease with increased hardness [22]. The specimen diameter is not measured continuously during these tests, so the true stress-plastic strain curves are only valid until necking of the specimen. The results from the SHTB tests are shown in Figure 15a), where they are compared to the result from a representative quasi-static test. It is seen that both the initial yield stress and the subsequent flow stress increase with increased strain rate. The most common material models incorporating strain-rate sensitivity use the assumption that the dynamic flow stress σ_d has a log-linear dependence of the strain rate $\dot{\epsilon}$. To check this assumption the ratio σ_d / σ_s , where σ_s is the quasi-static flow stress, is plotted against the strain rate in Figure 15b) for various levels of plastic strain. As the strain increases, the ratio σ_d / σ_s converges towards a linear dependency on the strain rate plotted on a logarithmic scale. The deviation at the initial yield stress and at 2% plastic strain is reasonable, as the SHTB test requires a certain number of reflections of the elasto-plastic stress waves in

the specimen before stress equilibrium is obtained. In any case, Figure 15 indicates that the strain-rate sensitivity of the unhardened material is moderate. It is therefore likely to assume that the strain-rate sensitivity for the hardened materials is low.

5 Metallurgical investigations

To gain a deeper understanding of the different deformation and fracture processes occurring during impact, fracture surfaces of several of the projectiles used in the Taylor impact tests were examined in a scanning electron microscope (SEM). In addition, the initial microstructure of the different hardened materials was investigated in a light optical microscope. The main results from the metallurgical investigations are presented in the following.

Figure 16 shows the microstructure in the central part of the projectiles at the different hardness values. In the two hardened projectiles a martensitic structure is observed with a dense distribution of retained spheroidized cementite. In the HRC 52 projectile these cementite grains are found along the former austenite grain boundaries. Based on the differences in mechanical properties observed between the tensile test specimens cut from the bulk material before and after hardening, the microstructure of the tensile test specimens cut before hardening was investigated as well. Figure 17 shows the microstructure in a cross-section perpendicular to the longitudinal direction for a representative specimen for each hardness value. The microstructure here is clearly more uniform than the microstructure of the projectiles, and it is also seen by comparing Figure 16 and Figure 17 that the problem with cementite on the grain boundaries is avoided in the tensile test specimens cut before hardening. This confirms that the faster and more uniform cooling of these specimens prohibits precipitation of carbides and thus helps explaining the difference in mechanical behaviour.

For the unhardened projectiles, the projectile that impacted at 341.4 m/s was investigated because it was the only one that fractured during testing. This projectile was already presented in Figure 8, and some fractographs are given in Figure 18. The fractographs show fracture surfaces from two different cracks in the projectile, and it is evident that a dimpled structure due to void growth and coalescence dominate the surfaces. This indicates a ductile fracture in these projectiles.

Among the HRC 40 projectiles, the one that impacted at 297.1 m/s was chosen for SEM inspections. In this case, one of the pieces that broke off during impact was analysed. The

projectile is shown in Figure 9, while some fractographs are given in Figure 19. From these fractographs it is seen that there is more variation in the fracture surfaces for the HRC 40 projectile, although the failure modes are similar to those in the unhardened projectile at the macroscopic level. The fracture process is found to be a mixture of ductile fracture identified by the dimpled structure caused by voids and brittle fracture identified by the flat surfaces with cleavage-like patterns.

For the HRC 52 projectiles, several interesting modes were observed already at the macroscopic level. The HRC 52 projectile that impacted at 132.9 m/s and fractured with a principal shear crack had a distinct glassy surface at the fracture plane. Also the projectile that fragmented at an impact velocity of 201.8 m/s showed the same glassy surface in conical-shaped fragments that were originally at the impact end of the projectile. Both instances of glassy surfaces are shown in Figure 20.

Several of the fragments from the projectile that impacted at 201.8 m/s were chosen for a closer inspection in the SEM. A wide variety of fracture surfaces was found in these fragments. Some fracture surfaces from the front of the projectile are shown in Figure 21 and Figure 22. In Figure 21 it is seen that voids are absent, and a smooth fracture surface appears. This is a clear evidence of a brittle fracture. Figure 22 presents possible melted and solidified material found in the principal shear fracture surface. This can be interpreted as an evidence of extremely high temperatures in the highly localised shear zones due to adiabatic heating. It is worth noting that no evidence of high temperatures was found in the HRC 52 projectiles at global level, unlike the blue brittleness indicating elevated global temperatures in the unhardened and HRC 40 projectiles. Figure 23 shows the fracture surfaces in a fragment some distance from the impacting end of the HRC 52 projectile that experienced fragmentation (see also Figure 10). It is seen that in this part of the projectile the fracture process is completely different. The fracture surface here is dominated by voids with some cleavage-like patterns and facets, indicating a quasi-cleavage form of fracture.

The main conclusion from the metallurgical study is that the various deformation and fracture modes occurring during impact can be explained from fractographic observations. For the unhardened projectiles, the deformation and fracture process is ductile and controlled by nucleation, growth and coalescence of voids. For HRC 40 projectiles, a combined ductile-brittle fracture process is observed, since both dimples and cleavage are present. The fragmentation process is mainly brittle for HRC 52 projectiles, with cleavage as the dominating fracture mode, even though more ductile fracture modes are found further away from the impacting end of the projectile. The temperature increase due to adiabatic heating seems to be prominent, since both

the unhardened and the HRC 40 projectiles show blue brittleness, while evidence of melted and solidified material is present for the HRC 52 projectile. The latter indicates that the local temperature has been in the order of 1500 °C during impact.

6 Discussion

From the experimental programme presented above, various deformation and fracture modes were obtained dependent on the impact velocity and projectile hardness. For impact velocities below the critical velocity, all projectiles mushroomed by plastic deformation. The critical impact velocities were found to be 297 m/s (unhardened), 247 m/s (HRC 40) and 124 m/s (HRC 52), as indicated in Table 3. Above these critical velocities, failure was always obtained within the limitations of this study. The dominant fracture mode for the most ductile projectiles, i.e. the unhardened and the HRC 40 projectiles, was a combination of tensile splitting and spiral shear, while for the more brittle HRC 52 projectile the dominant fracture mode was principal shear fracture or full fragmentation. These fracture modes were confirmed by the metallurgical study and affirm the modes observed by Xiao et al. [14] for respectively ductile and brittle projectiles, except that extensive petalling was not observed. Extensive void growth [11] was not observed in any of the present experiments.

The metallurgical investigation revealed that principal shear fracture was prominent also in the HRC 52 projectiles that fragmented, while the fragmentation process itself is caused by quasi-cleavage. This offers experimental support to the numerical findings by Xiao et al. [15] relating fragmentation to shear mechanisms, at least in the front of the projectile. In addition to the three fracture surfaces also observed by Ren et al. [16], surfaces indicating a quasi-cleavage form of fracture were found in the metallurgical investigation. Contrary to the separation of fracture surfaces by velocity observed in [16], the different fracture surfaces observed here are determined by the material type.

One major concern in this study is the considerable difference in material properties between the tensile tests first hardened then cut and those first cut then hardened (see Figure 13 and Figure 14). Firstly, to check the homogeneity of the hardness through the radial direction, microhardness measurements were carried out over the cross-section of both projectiles and tensile test specimens hardened to HRC 40 and HRC 52, respectively. The hardness was measured along three paths across the same sample. For the hardened projectiles, the cross-section was located 10 mm from the rear-side end, while for the tensile test specimens the cross-section was taken in the centre of the gauge area. The paths were named axis 1, 2 and 3, and

their positions are shown in Figure 24. The hardness was measured in a Reicherter Brivisor KL2 using the HV10 Vickers scale and the measured variations of the hardness along these profiles are displayed in Figure 25. From the results, one observes that the hardness is higher in the projectiles than in the tensile test specimens with the same nominal hardness. This confirms the significant role on the mechanical properties of the material the cooling rate of the specimens after hardening may play.

When the steel is heated to the hardening temperature, the matrix is transformed from ferrite/pearlite to austenite, for which the solubility of carbon and carbide-forming alloying elements is higher. Thus, carbides will dissolve into the matrix giving the hardening effect. If the steel is quenched sufficiently rapidly after the hardening process, the carbon atoms do not have time to reposition themselves to reform ferrite/pearlite, i.e. they are locked in position, and martensite is formed. If the steel has not been held for long enough time at the hardening temperature or if the temperature has not been high enough, it is possible to obtain some retained cementite as observed in Figure 16 [23]. From the continuous cooling transformation (CCT) diagram of tool steels (see [24]), it can be seen that if the quenching rate from austenite is too low, pearlite and bainite will be formed and carbides may precipitate along the grain boundaries before the matrix is transformed to martensite. This is known to be detrimental to the mechanical properties of the hardened steel [24], and may be the case for some of the tensile specimens that have been cut from the hardened projectile. In Figure 17 the microstructure in the central part of the tensile test specimens at HRC 40 and HRC 52 was shown. If compared to the corresponding images from the projectiles in Figure 16, it is clearly seen that the retained cementite particles, especially in HRC 52, are distributed much more evenly in the matrix in the tensile test specimen, whereas in the projectile the cementite is found along old austenite grain boundaries. This alignment may cause a more brittle behaviour of the tensile specimens. Thus, the difference in mechanical properties between the projectiles and the tensile specimens is explained by the longer cooling time for the projectiles. However, it is also observed from Figure 25 that the distance to the surface has no significant influence on the hardness. This indicates that heat conduction maintains a homogeneous temperature field in the projectiles during cooling. Accordingly, the conjecture put forward in Section 4.1 implying a correlation of the mechanical properties with the radial distance from the surface is not confirmed. It is therefore assumed that the variations seen are of an entirely stochastic nature.

Another observation from the microhardness measurements is that the scatter is in the order of 10% of the average value for both the HRC 40 and HRC 52 projectiles. For the tensile test specimen that has a much more even microstructure according to Figure 17, the scatter is

smaller but still 5%. This combined with the scatter in failure strain demonstrated in the tensile tests, promotes a stochastic variable approach to numerical modelling of fracture and fragmentation in hardened projectiles during impact against hard and thick target plates.

7 Conclusions

The main conclusions from this study may be summarized as follows:

- A critical impact velocity was observed for all three materials. Below this critical velocity, only plastic deformation in form of mushrooming took place, while above this critical velocity various types of fracture occurred.
- The dominant fracture mode for the most ductile projectiles (UH and HRC 40) was a combination of tensile splitting and spiral shear, while for the more brittle projectiles (HRC 52) the dominant fracture mode was principal shear fracture or full fragmentation.
- For the unhardened projectiles, the fracture process was ductile and controlled by nucleation, growth and coalescence of voids. For HRC 40 projectiles, a combined ductile-brittle fracture process was obtained, since both dimpled fracture surfaces and cleavage were observed. The fragmentation process was mainly brittle for HRC 52 projectiles, with cleavage as the dominating mechanism.
- The temperature increase due to adiabatic heating seemed to be prominent, since both the unhardened and the HRC 40 projectiles showed blue brittleness, while evidences of melted and solidified material were present in the HRC 52 projectiles.
- Several series of tensile tests were carried out. A considerable spread in mechanical properties between the test specimens first hardened then cut and the test specimens first cut then hardened was found. The reason for this spread is caused by the different cooling rates during hardening of samples with different size. For the hardened projectiles a too low cooling rate may cause carbide precipitation along the grain boundaries, which is detrimental to the mechanical behaviour of the material.
- The hardened materials studied here have a stochastic variation in the mechanical properties. It is thus important to include this variation in the analysis of ballistic impact where fracture and fragmentation in the projectile may occur.

Acknowledgement

The financial support of this work from the Structural Impact Laboratory (SIMLab), Centre for Research-based Innovation (CRI) at the Norwegian University of Science and Technology (NTNU), is gratefully acknowledged. The authors would like to express their gratitude to Professor Jan Ketil Solberg for fruitful discussions on the metallurgical studies and to Dr. Fredrik Haakonsen for conducting the hardening of the materials. We also acknowledge Mr. Martin Kristoffersen, Mr. Even Zachariassen, Mr. Terje Karlsen and Mr. Andreas Bjune Kjølseth for their contributions during the experimental tests.

References

- [1] Børvik T, Hopperstad OS, Langseth M, Malo KA. Effect of target thickness in blunt projectile penetration of Weldox 460 E steel plates. *Int J Impact Eng* 2003;28:413-64.
- [2] Dey S, Børvik T, Hopperstad OS, Leinum JR, Langseth M. The effect of target strength on the perforation of steel plates using three different projectile nose shapes. *Int J Impact Eng* 2004;30:1005-38.
- [3] Dey S, Børvik T, Teng X, Wierzbicki T, Hopperstad OS. On the ballistic resistance of double-layered steel plates: An experimental and numerical investigation. *Int J Solids Struct* 2007;44:6701-23.
- [4] Dey S, Børvik T, Hopperstad OS. Computer-aided design of protective structures: Numerical simulations and experimental validation. *Appl Mech Mater* 2011;82:686-91.
- [5] Taylor G. The Use of Flat-Ended Projectiles for Determining Dynamic Yield Stress. I. Theoretical Considerations. *Proc R Soc Lon Ser-A* 1948;194:289-99.
- [6] Whiffin AC. The Use of Flat-Ended Projectiles for Determining Dynamic Yield Stress. II. Tests on Various Metallic Materials. *Proc R Soc Lon Ser-A* 1948;194:300-22.
- [7] Carrington WE, Gayler MLV. The Use of Flat-Ended Projectiles for Determining Dynamic Yield Stress. III. Changes in Microstructure Caused by Deformation under Impact at High-Striking Velocities. *Proc R Soc Lon Ser-A* 1948;194:323-31.
- [8] Johnson W. *Impact Strength of Materials*. London: Edward Arnold, Ltd; 1972.
- [9] Teng X, Wierzbicki T, Hiermaier S, Rohr I. Numerical prediction of fracture in the Taylor test. *Int J Solids Struct* 2005;42:2929-48.

- [10] Backman ME, Goldsmith W. The mechanics of penetration of projectiles into targets. *J Eng Sci* 1978;16:1-99.
- [11] Woodward RL, O'Donnell RG, Flockhart CJ. Failure mechanisms in impacting penetrators. *J Mater Sci* 1992;27:6411-6.
- [12] Chen XW, Chen G, Zhang FJ. Deformation and Failure Modes of Soft Steel Projectiles Impacting Harder Steel Targets at Increasing Velocity. *Exp Mech* 2008;48:335-54.
- [13] Karlsen T, Kjølseth AB. Fragmentation of Metallic Materials During Impact. [MSc Thesis]. Trondheim, Norway: Norwegian University of Science and Technology; 2012.
- [14] Xiao X, Zhang W, Wei G, Mu Z. Effect of projectile hardness on deformation and fracture behavior in the Taylor impact test. *Mater Design* 2010;31:4913-20.
- [15] Xiao X, Zhang W, Wei G, Mu Z, Guo Z. Experimental and numerical investigation on the deformation and failure behavior in the Taylor test. *Mater Design* 2011;32:2663-74.
- [16] Ren Y, Tan C, Zhang J, Wang F. Dynamic fracture of Ti-6Al-4V alloy in Taylor impact test. *T Nonferr Metal Soc* 2011;21:223-35.
- [17] Børvik T, Hopperstad OS, Berstad T, Langseth M. A computational model of viscoplasticity and ductile damage for impact and penetration. *Eur J Mech A-Solid* 2001;20:685-712.
- [18] Dieter GE. *Mechanical metallurgy*. London: McGraw-Hill; 1988.
- [19] ISO 6892-1:2009. *Metallic materials - Tensile testing - Part 1: Method of test at room temperature*. Geneva, Switzerland; 2009.
- [20] Clausen AH, Børvik T, Hopperstad OS, Benallal A. Flow and fracture characteristics of aluminium alloy AA5083-H116 as function of strain rate, temperature and triaxiality. *Mat Sci Eng A-Struct* 2004;365:260-72.
- [21] ISO 26203-1:2010. *Metallic materials - Tensile testing at high strain rates - Part 1: Elastic-bar-type systems*. Geneva, Switzerland; 2010
- [22] Børvik T, Dey S, Clausen AH. Perforation resistance of five different high-strength steel plates subjected to small-arms projectiles. *Int J Impact Eng* 2009;36:948-64.
- [23] Luzginova N, Zhao L, Sietsma J. Evolution and thermal stability of retained austenite in SAE 52100 bainitic steel. *Mat Sci Eng A-Struct* 2007;448:104-10

- [24] Uddeholm.com [Internet]. Hagfors, Sweden: Uddeholms AB; c2011 [updated 2012 Jun; cited 2012 Dec 6]. Heat treatment of tool steel; [pdf, 20 pages]. Available from: <http://www.uddeholm.com/files/heattreatment-english.pdf>

List of Tables

Table 1: Nominal chemical composition (in weight %) of Arne tool steel.

Table 2: Heat-treatment processes of Arne tool steel projectiles.

Table 3: Some experimental results.

Table 4: Fragment-size distribution (in weight %) after impact.

Table 5: Heat-treatment processes of Arne tool steel tensile test specimens.

Table 1: Nominal chemical composition (in weight %) of Arne tool steel.

C	Si	Mn	Cr	W	V
0.95	0.30	1.10	0.60	0.60	0.10

Table 2: Heat-treatment processes of Arne tool steel projectiles.

Hardness	Hardening	Cooling	Tempering	Cooling
HRC 40	45 min at 800°C in furnace at normal atmosphere	Oil at 30-140°C + air	2 × 1.5 h at 530°C	Air
HRC 52	45 min at 800°C in furnace at normal atmosphere	Oil at 30-140°C + air	2 × 1.5 h at 340°C	Air

Table 3: Some experimental results.

Hardness (HRC)	Impact velocity (m/s)	Deformed diameter (mm)	Deformed length (mm)	Fracture mode
UH	126.7	22.5	76.0	Mushrooming
	155.5	23.8	74.0	Mushrooming
	185.5	25.6	71.8	Mushrooming
	196.7	26.6	71.1	Mushrooming
	250.0	30.5	67.0	Mushrooming
	297.2	35.1	62.2	Mushrooming
	341.4	-	-	Spiral shear
HRC 40	132.5	22.1	77.5	Mushrooming
	137.1	22.2	77.4	Mushrooming
	182.8	24.6	75.3	Mushrooming
	201.2	25.9	74.4	Mushrooming
	246.5	28.8	72.2	Mushrooming
	269.6	30.5	70.9	Tensile splitting
	297.7	-	-	Spiral shear
	325.6	-	-	Spiral shear
	356.5	-	-	Spiral shear
HRC 52	124.4	22.5	78.8	Mushrooming
	132.9	-	-	Principal shear
	134.7	-	-	Principal shear
	153.7	-	-	Fragmentation
	201.8	-	-	Fragmentation
	250.5	-	-	Fragmentation
	296.3	-	-	Fragmentation

Table 4: Fragment-size distribution (in weight %) after impact.

Hardness (HRC)	Impact velocity (m/s)	Fragment size (mm)					
		> 8	8-4	4-2	2-1	1-0.5	< 0.5
HRC 40	297.7	99.44	0.54	0.02	-	-	-
	325.6	100.00	-	-	-	-	-
	356.6	99.55	0.45	-	-	-	-
HRC 52	132.9	100.00	-	-	-	-	-
	134.7	97.34	1.91	0.69	0.04	0.02	-
	153.7	92.05	6.70	1.18	0.07	-	-
	201.8	83.85	11.67	1.88	0.97	1.04	0.59
	250.5	79.94	14.24	4.69	0.72	0.28	0.13
	296.3	58.48	25.87	11.04	2.97	1.04	0.60

Table 5: Heat-treatment processes of Arne tool steel tensile test specimens.

Hardness	Hardening	Cooling	Tempering	Cooling
HRC 40	25 min at 800°C in furnace at argon-gas atmosphere	Liquid salt at 180°C + air	2 × 1.5 h at 530°C	Air
HRC 52	25 min at 800°C in furnace at argon-gas atmosphere	Liquid salt at 180°C + air	2 × 1.5 h at 340°C	Air

List of Figures

- Figure 1: Deformation and fracture modes in the Taylor bar impact test [13].**
- Figure 2: Sketch of the compressed gas gun used in the Taylor bar impact tests.**
- Figure 3: Typical high-speed video images from Taylor bar impact tests with projectiles having different hardness at an impact velocity of $v_i \approx 300$ m/s.**
- Figure 4: Unhardened projectile after impact at 297.2 m/s.**
- Figure 5: Microscopic images of the unhardened projectile after impact at 297.2 m/s. (a) The projectile has been sliced in the longitudinal direction, showing no sign of void growth in the central part. (b) Evidence of a deformed sulphide that has partly dissolved from the etching process during preparation.**
- Figure 6: HRC 52 projectile impacting at 132.9 m/s captured by the high-speed video camera. The fracture mode is principal shear fracture.**
- Figure 7: HRC 52 projectile impacting at 134.7 m/s captured by the high-speed video camera. Two shear fractures are evident.**
- Figure 8: Unhardened projectile after impact at 341.4 m/s. A combination of spiral shear cracks and tensile splitting is visible.**
- Figure 9: HRC 40 projectile after impact at 297.1 m/s. A combination of spiral shear cracks and tensile splitting is visible.**
- Figure 10: HRC 52 projectile after impact at 250.5 m/s. The fragments are sorted according to their size.**
- Figure 11: Test geometries of (a) specimens used in the quasi-static tests, and (b) specimens used in the dynamic tests.**
- Figure 12: True stress versus true strain curves from quasi-static tensile tests on specimens from unhardened material.**
- Figure 13: True stress versus true strain curves from quasi-static tensile tests on specimens from material hardened to HRC 40.**
- Figure 14: True stress versus true strain curves from quasi-static tensile tests on specimens from material hardened to HRC 52.**
- Figure 15: (a) True stress – plastic strain curves at elevated strain-rates and room temperature, (b) the flow-stress ratio σ_d / σ_s versus strain rate on logarithmic scale for various levels of plastic strain.**
- Figure 16: Microstructure in the central part of the projectile at different hardness values.**
- Figure 17: Microstructure in the central part of the tensile test specimens cut and then hardened to HRC 40 and HRC 52.**
- Figure 18: SEM images of fracture surfaces of unhardened projectile that impacted at 341.4 m/s.**
- Figure 19: SEM images of fracture surfaces of HRC 40 projectile that impacted at 297.1 m/s.**
- Figure 20: Glassy surfaces observed in HRC 52 projectiles. (a) The projectile that fractured with a principal shear fracture. (b) The projectile that fragmented.**
- Figure 21: SEM images of the glassy fracture surfaces of the HRC 52 projectile that impacted at 201.8 m/s.**

Figure 22: SEM images of a fracture surface of the HRC 52 projectile that impacted at 201.8 m/s showing melted and solidified material.

Figure 23: SEM images of fracture surfaces in a fragment of the HRC 52 projectile that impacted at 201.8 m/s some distance from the impacting end displaying quasi-cleavage.

Figure 24: Position of measured profiles over the cross-section

Figure 25: Measured hardness over the cross-sections of a) HRC 40 projectiles, b) HRC 52 projectiles, c) HRC 40 tensile specimens and d) HRC 52 tensile specimens.

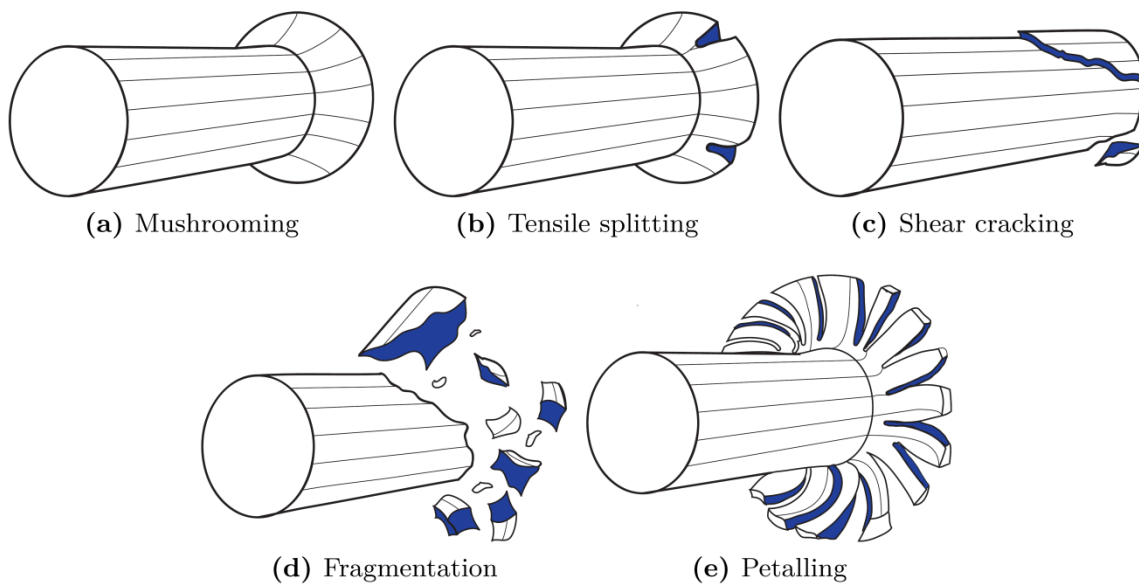


Figure 1: Deformation and fracture modes in the Taylor bar impact test [13].

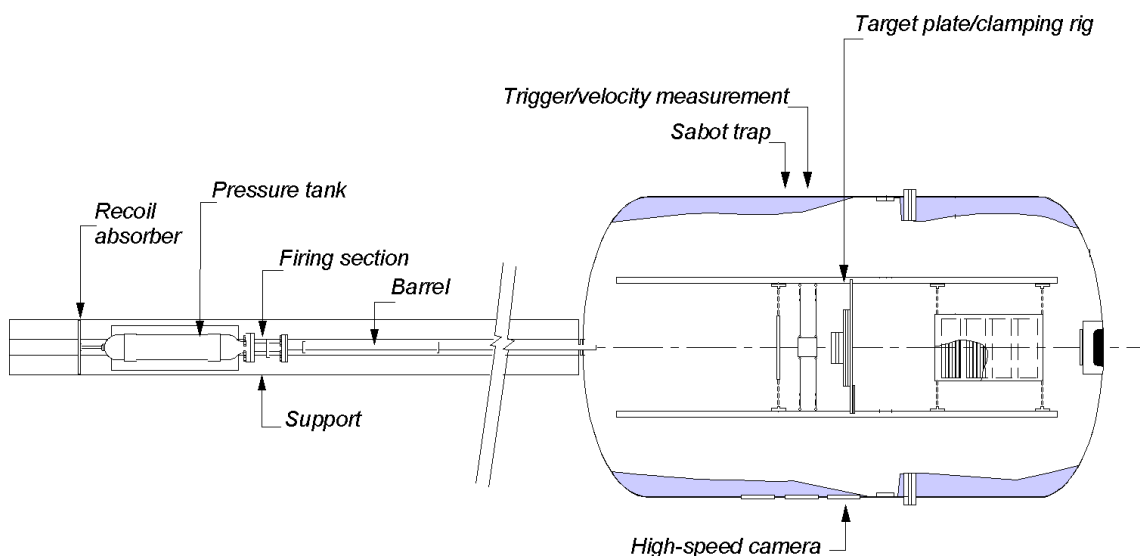
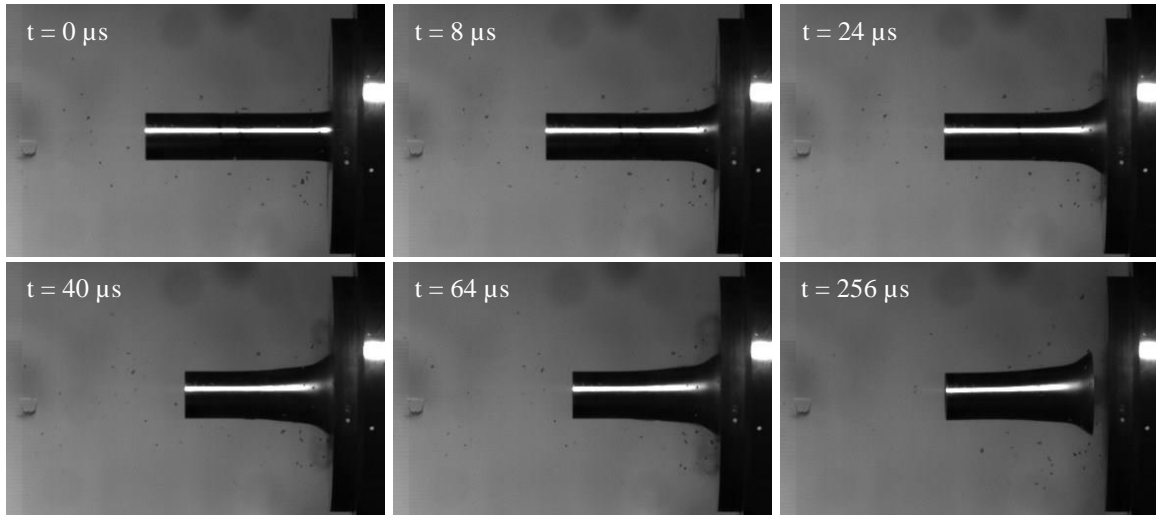
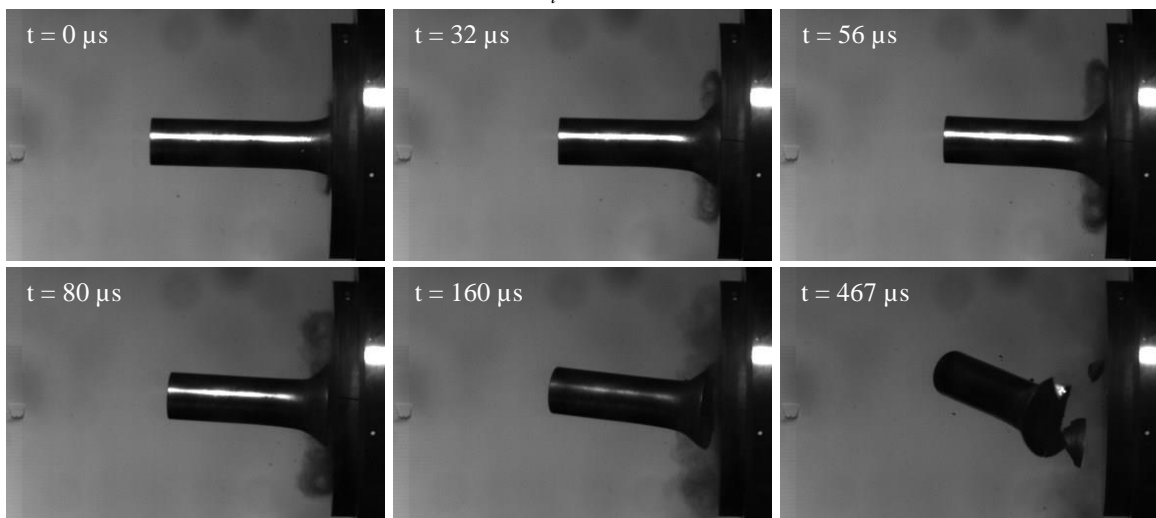


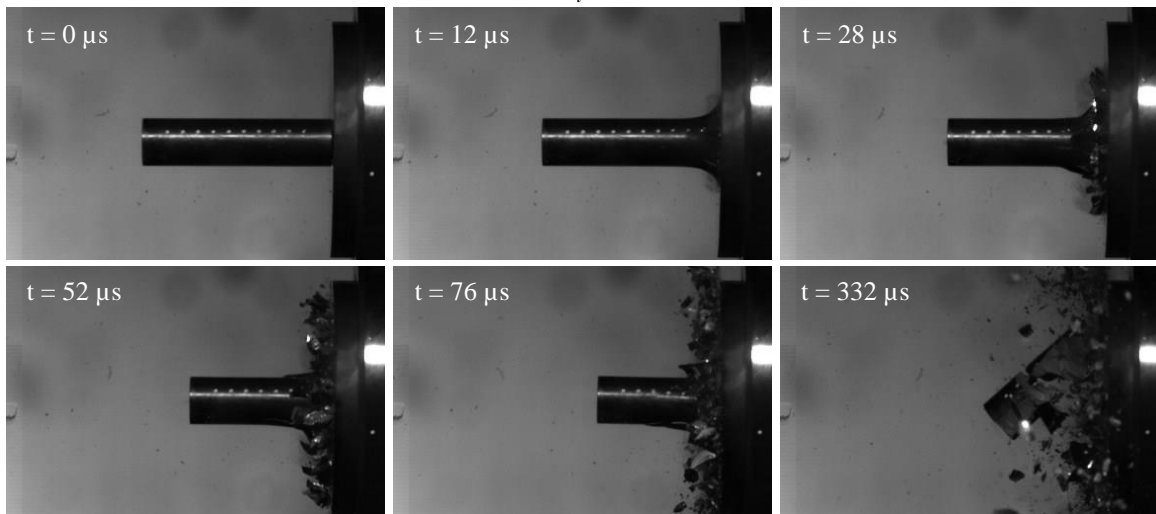
Figure 2: Sketch of the compressed gas gun used in the Taylor bar impact tests.



(a) UH - $v_i = 297.2$ m/s



(b) HRC 40 - $v_i = 297.7$ m/s



(c) HRC 52 - $v_i = 296.9$ m/s

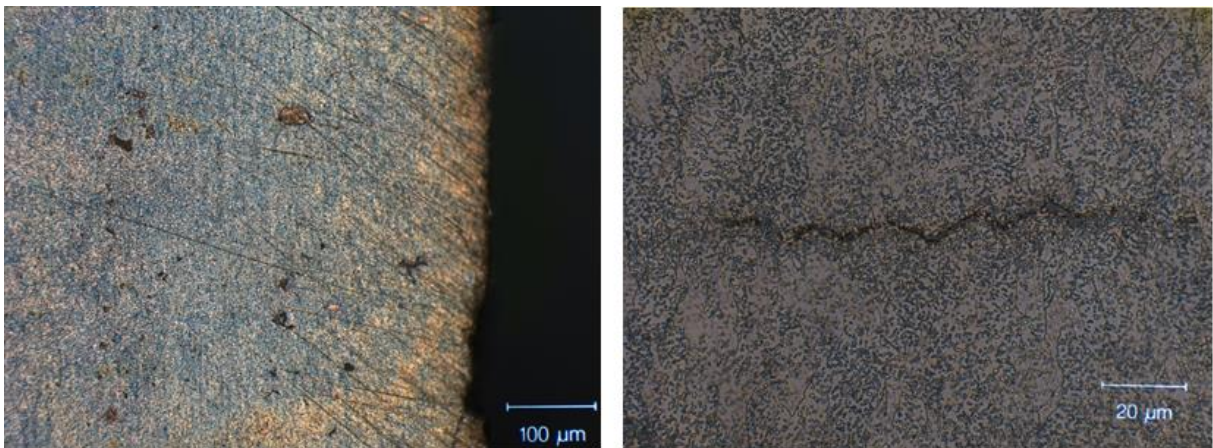
Figure 3: Typical high-speed video images from Taylor bar impact tests with projectiles having different hardness at an impact velocity of $v_i \approx 300$ m/s.



(a) Overview

(b) Impact end

Figure 4: Unhardened projectile after impact at 297.2 m/s.



(a) Overview

(b) Detail

Figure 5: Microscopic images of the unhardened projectile after impact at 297.2 m/s. (a) The projectile has been sliced in the longitudinal direction, showing no sign of void growth in the central part. (b) Evidence of a deformed sulphide that has partly dissolved from the etching process during preparation.

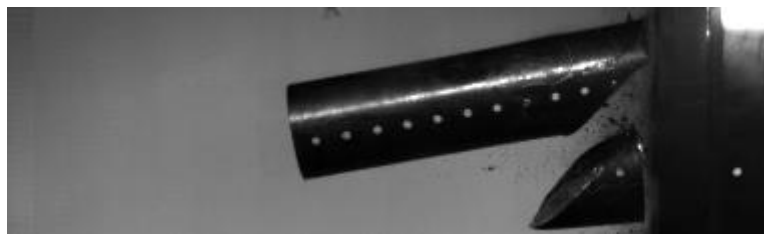


Figure 6: HRC 52 projectile impacting at 132.9 m/s captured by the high-speed video camera. The fracture mode is principal shear fracture.



Figure 7: HRC 52 projectile impacting at 134.7 m/s captured by the high-speed video camera. Two shear fractures are evident.



(a) Overview

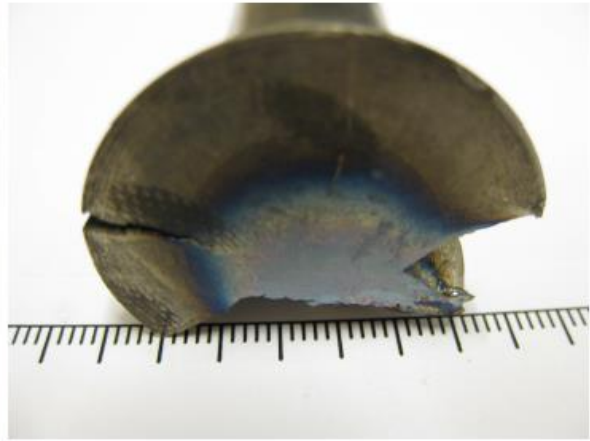


(b) Impact end

Figure 8: Unhardened projectile after impact at 341.4 m/s. A combination of spiral shear cracks and tensile splitting is visible.



(a) Overview



(b) Impact end

Figure 9: HRC 40 projectile after impact at 297.1 m/s. A combination of spiral shear cracks and tensile splitting is visible.



Figure 10: HRC 52 projectile after impact at 250.5 m/s. The fragments are sorted according to their size.

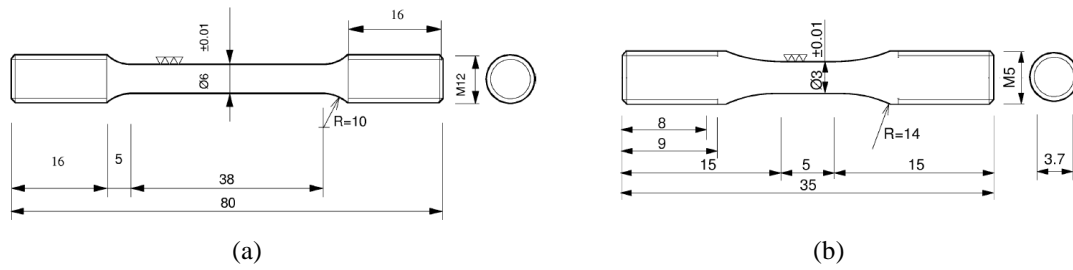


Figure 11: Test geometries of (a) specimens used in the quasi-static tests, and (b) specimens used in the dynamic tests.

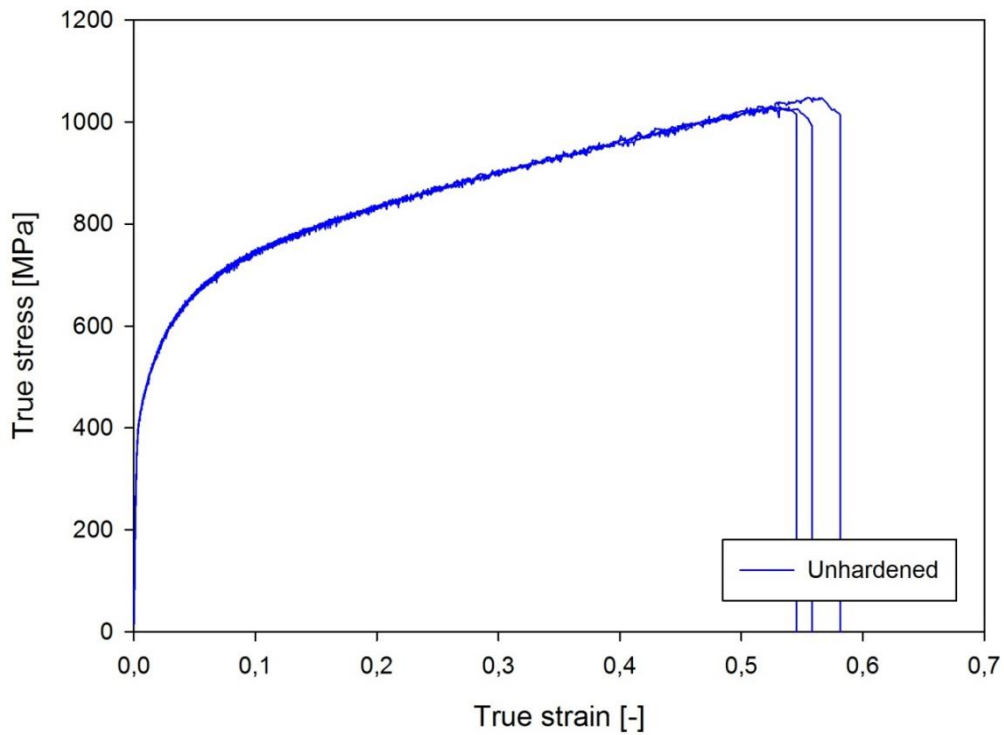


Figure 12: True stress versus true strain curves from quasi-static tensile tests on specimens from unhardened material.

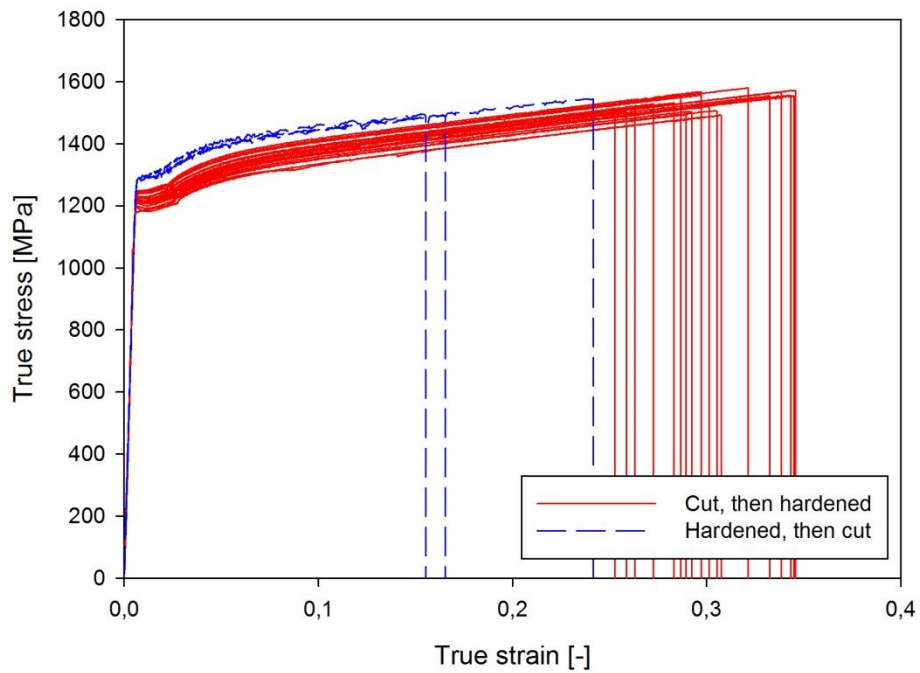


Figure 13: True stress versus true strain curves from quasi-static tensile tests on specimens from material hardened to HRC 40.

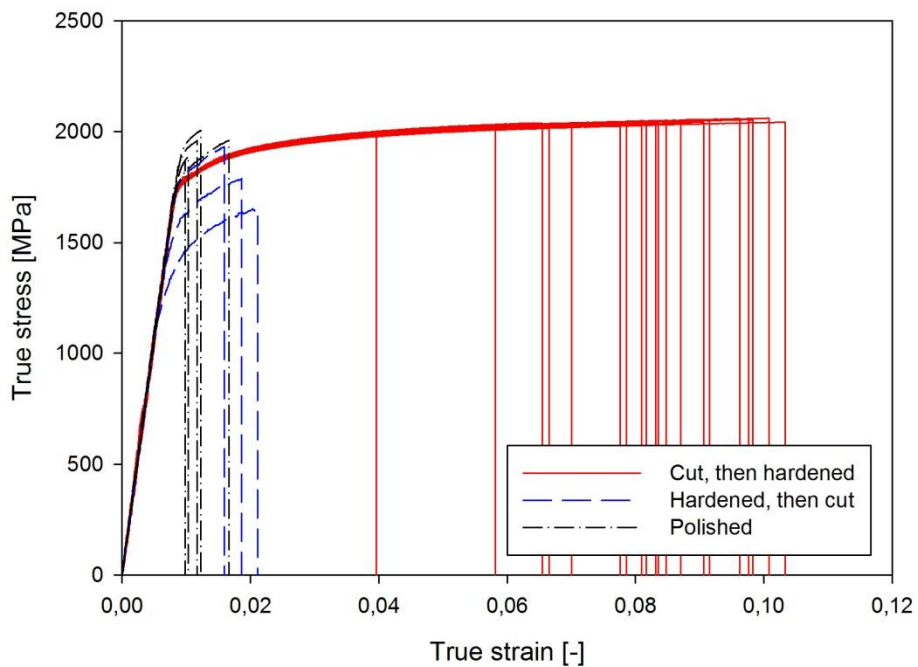


Figure 14: True stress versus true strain curves from quasi-static tensile tests on specimens from material hardened to HRC 52.

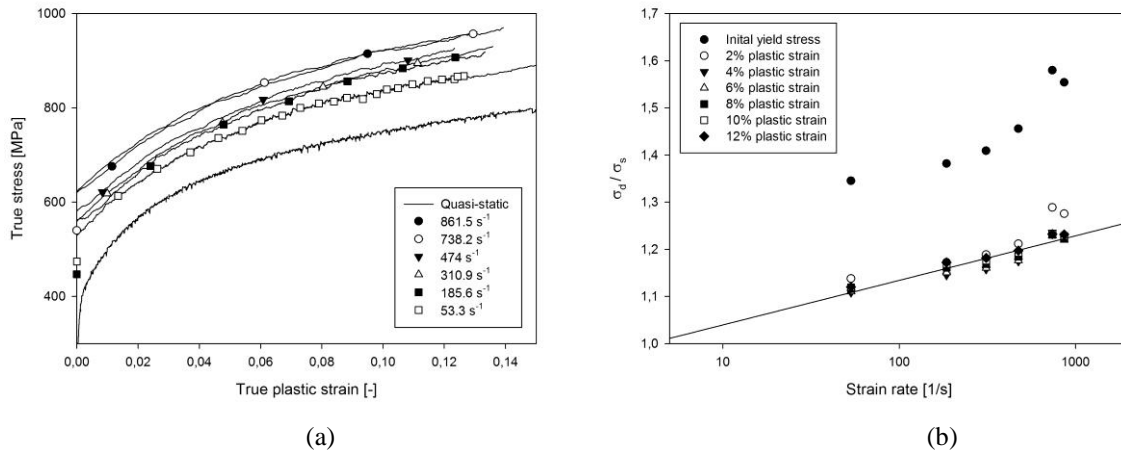


Figure 15: (a) True stress – plastic strain curves at elevated strain-rates and room temperature, (b) the flow-stress ratio σ_d / σ_s versus strain rate on logarithmic scale for various levels of plastic strain.

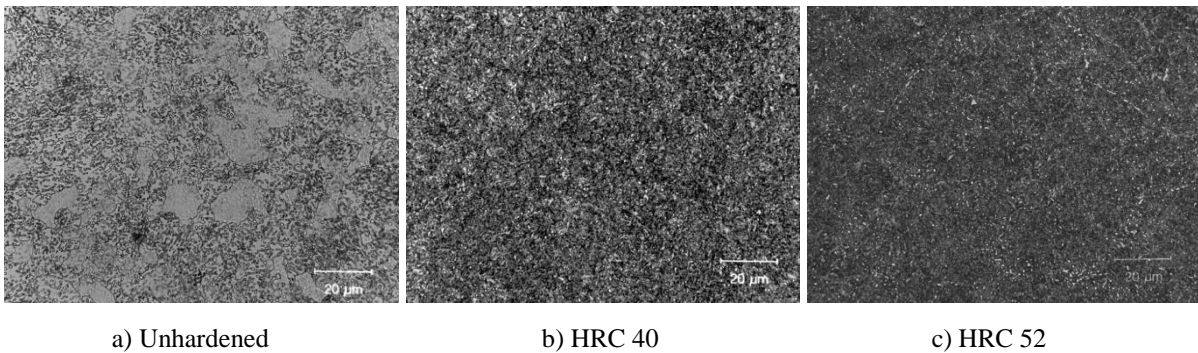


Figure 16: Microstructure in the central part of the projectile at different hardness values.

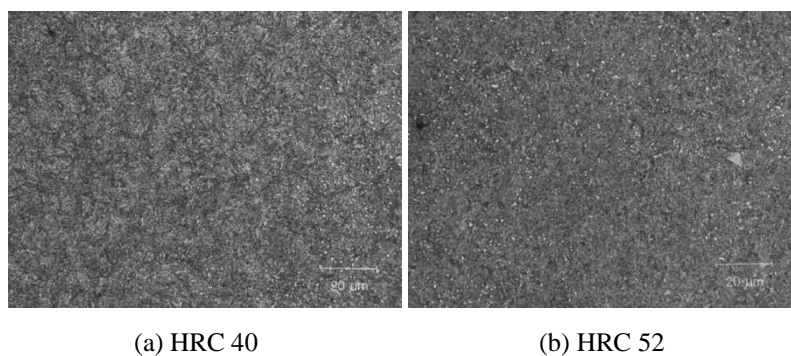
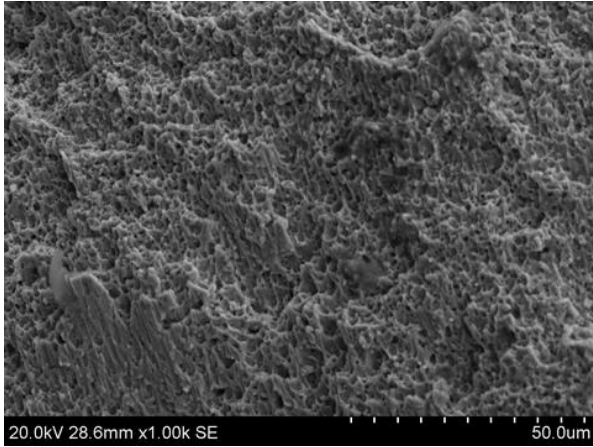
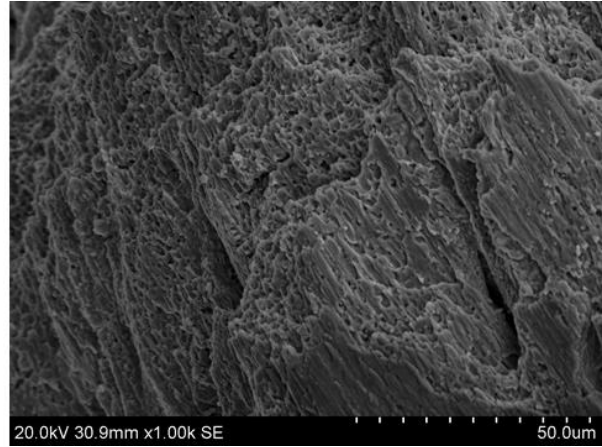


Figure 17: Microstructure in the central part of the tensile test specimens cut and then hardened to HRC 40 and HRC 52.

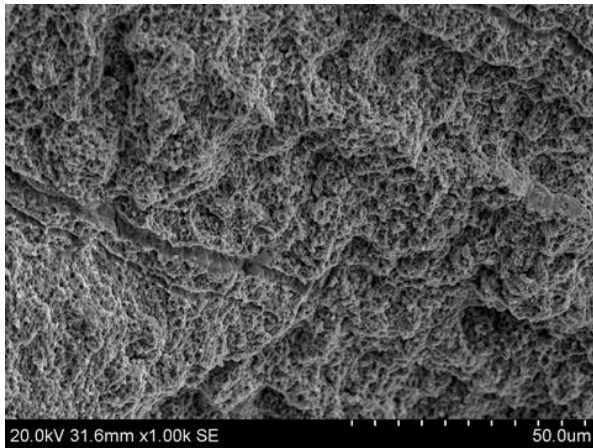


(a) Dimples

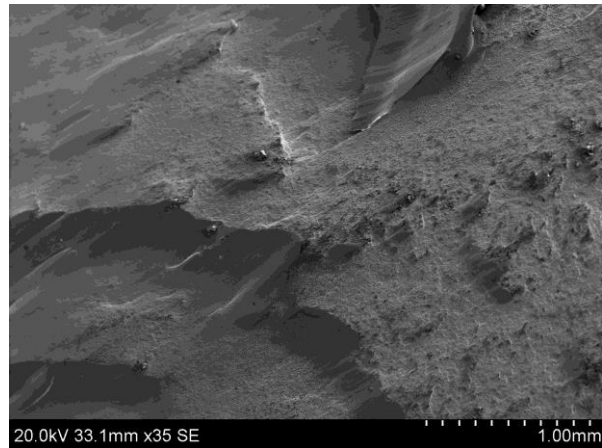


(b) Elongated dimples

Figure 18: SEM images of fracture surfaces of unhardened projectile that impacted at 341.4 m/s.



(a) Dimples



(b) Flat surface with cleavage-like patterns

Figure 19: SEM images of fracture surfaces of HRC 40 projectile that impacted at 297.1 m/s.



(a) Impacted at 132.9 m/s



(b) Impacted at 201.8 m/s

Figure 20: Glassy surfaces observed in HRC 52 projectiles. (a) The projectile that fractured with a principal shear fracture. (b) The projectile that fragmented.

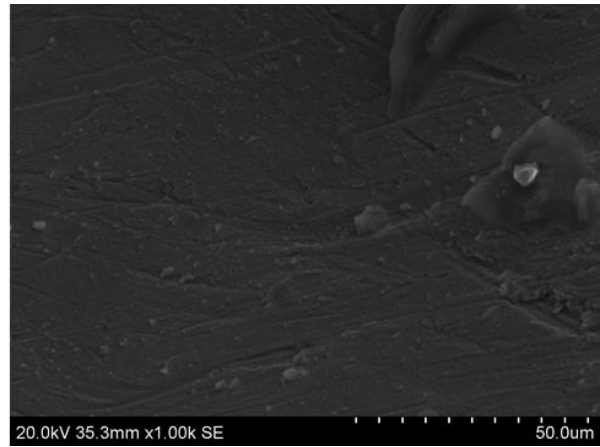
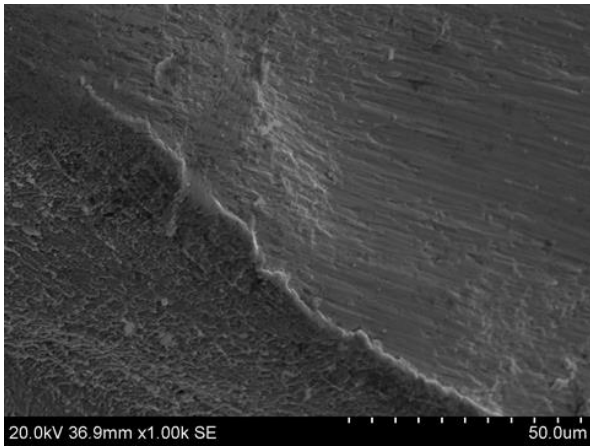


Figure 21: SEM images of the glassy fracture surfaces of the HRC 52 projectile that impacted at 201.8 m/s.

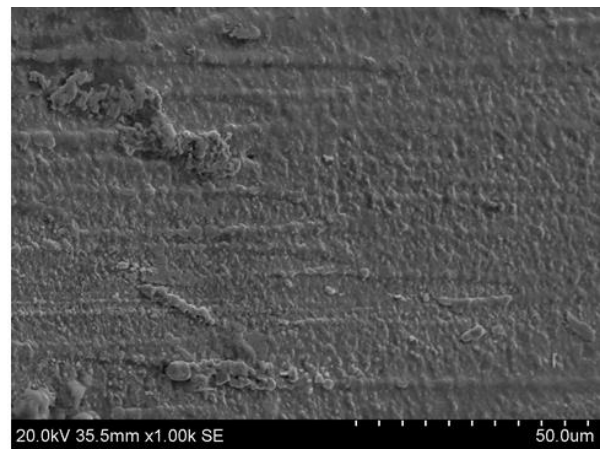
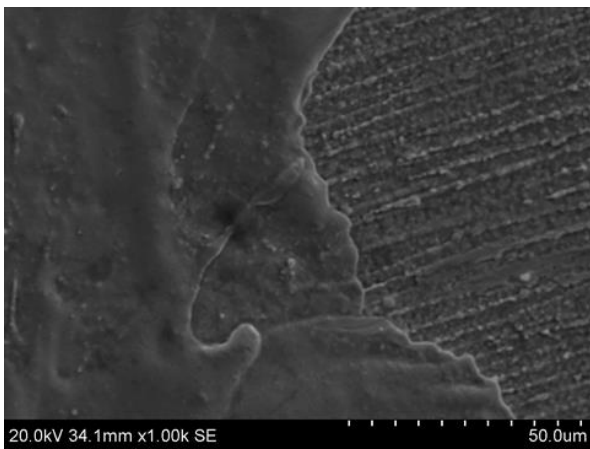


Figure 22: SEM images of a fracture surface of the HRC 52 projectile that impacted at 201.8 m/s showing melted and solidified material.

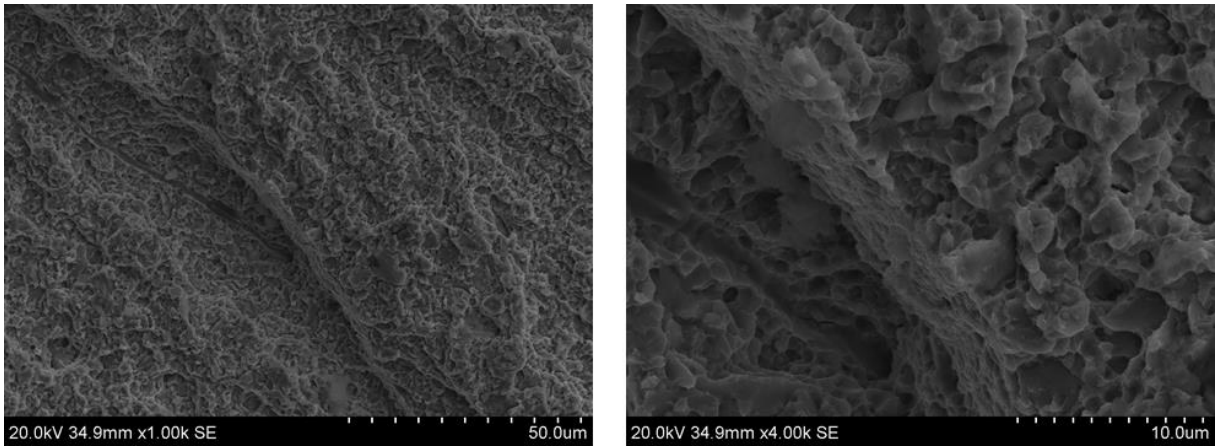


Figure 23: SEM images of fracture surfaces in a fragment of the HRC 52 projectile that impacted at 201.8 m/s some distance from the impacting end displaying quasi-cleavage.

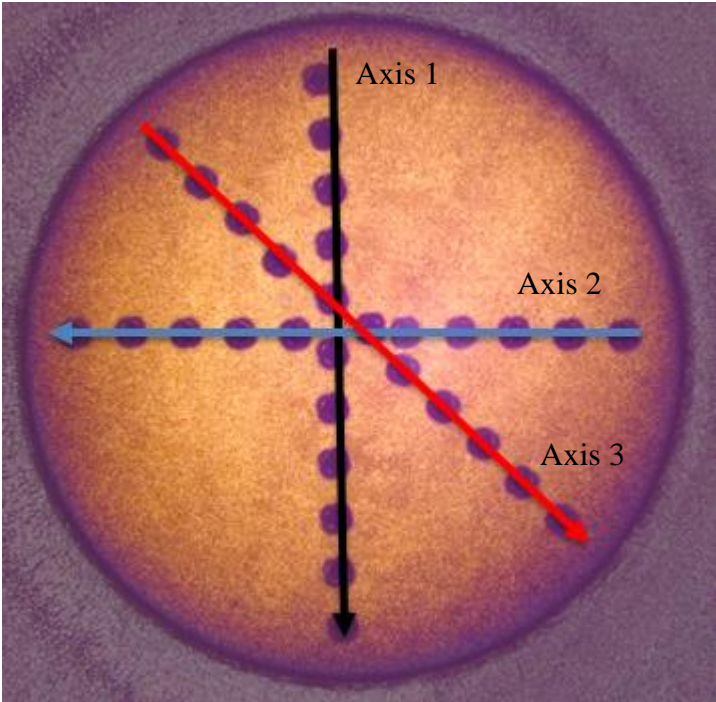
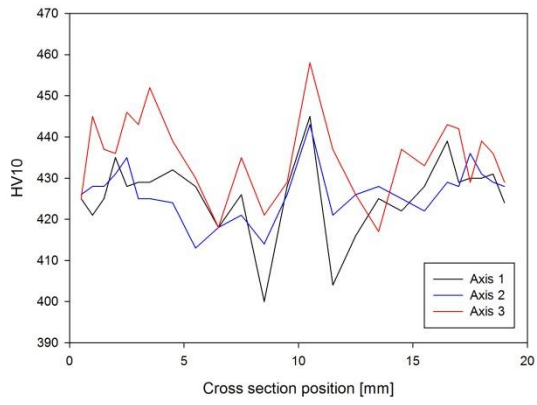
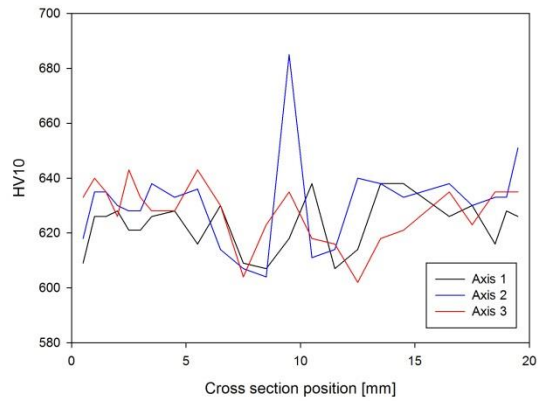


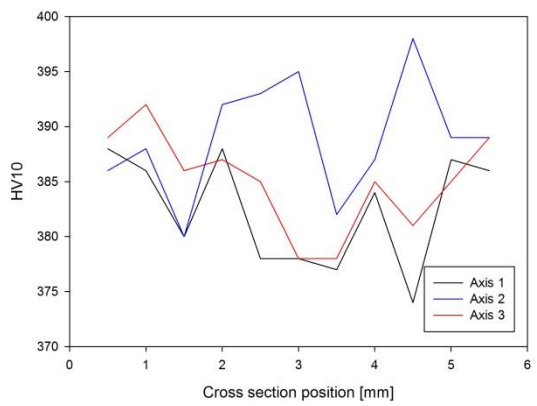
Figure 24: Position of measured profiles over the cross-section



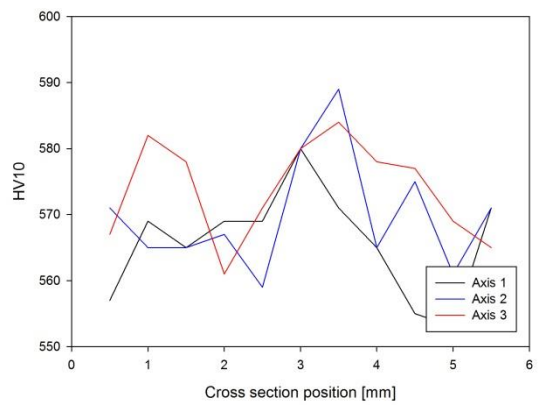
(a)



(b)



(c)



(d)

Figure 25: Measured hardness over the cross-sections of a) HRC 40 projectiles, b) HRC 52 projectiles, c) HRC 40 tensile specimens and d) HRC 52 tensile specimens.